Article

Frustration- and doping-induced magnetism in a Fermi–Hubbard simulator

https://doi.org/10.1038/s41586-023-06280-5

Received: 28 December 2022

Accepted: 2 June 2023

Published online: 2 August 2023

Check for updates

Muqing Xu[1], Lev Haldar Kendrick[1], Anant Kale[1], Youqi Gang[1], Geoffrey Ji[1], Richard T. Scalettar[2], Martin Lebrat[1] & Markus Greiner[1]✉

Geometrical frustration in strongly correlated systems can give rise to a plethora of novel ordered states and intriguing magnetic phases, such as quantum spin liquids[1–3]. Promising candidate materials for such phases[4–6] can be described by the Hubbard model on an anisotropic triangular lattice, a paradigmatic model capturing the interplay between strong correlations and magnetic frustration[7–11]. However, the fate of frustrated magnetism in the presence of itinerant dopants remains unclear, as well as its connection to the doped phases of the square Hubbard model[12]. Here we investigate the local spin order of a Hubbard model with controllable frustration and doping, using ultracold fermions in anisotropic optical lattices continuously tunable from a square to a triangular geometry. At half-filling and strong interactions $U/t \approx 9$, we observe at the single-site level how frustration reduces the range of magnetic correlations and drives a transition from a collinear Néel antiferromagnet to a short-range correlated 120° spiral phase. Away from half-filling, the triangular limit shows enhanced antiferromagnetic correlations on the hole-doped side and a reversal to ferromagnetic correlations at particle dopings above 20%, hinting at the role of kinetic magnetism in frustrated systems. This work paves the way towards exploring possible chiral ordered or superconducting phases in triangular lattices[8,13] and realizing t–t' square lattice Hubbard models that may be essential to describe superconductivity in cuprate materials[14].

The collective properties of spins with antiferromagnetic interactions crucially depend on the geometry of the lattice they inhabit[15]. On a square lattice, spins form a Néel order with antialigned neighbours; by contrast, their mutual antiparallel alignment cannot be satisfied on a triangular lattice, which is the simplest model for geometric frustration and features non-trivial spin order. This frustrated spin order is associated with a massive ground-state degeneracy with enhanced quantum fluctuations and may lead to exotic phases of matter, such as quantum spin liquids[1,2,16,17].

The Hubbard Hamiltonian is one of the most fundamental models describing the emergence of quantum magnetism among spin-1/2 electrons with kinetic energy t and interaction energy U. On the non-frustrated square lattice, it is thought to capture the essential physics of the strongly correlated electrons in the doped high-temperature superconducting cuprate materials[12]. Interpolating the Hubbard model between square and triangular lattices has important practical value to accurately describe a broader class of correlated materials with structural anisotropy, including layered organic compounds believed to host quantum spin liquid phases[3]. Anisotropic triangular Hubbard models would furthermore provide a minimal model to understand the competition between charge dopants and magnetism with frustration away from half-filling, for which much less is known, as numerical calculations are challenging owing to the absence of particle–hole symmetry.

Ultracold fermions in optical lattices form a pristine realization of the Hubbard model. They can be used for the quantum simulation of frustrated systems[18,19], shedding light on both its half-filled and doped phases with site-resolved observables. In this work, we realize a Fermi–Hubbard system with tunable frustration and investigate its magnetic order as a function of doping with single-site resolution in the regime of intermediate to strong interactions $U/t \approx 9$. We explicitly implement tunable tunnelling anisotropy and investigate the combined effect of frustration and doping on magnetic order at temperatures $T/t \lesssim 0.4$ comparable with or lower than the spin exchange energy. This is in contrast to concurrent work analysing nearest-neighbour antiferromagnetic correlations on an isotropic triangular lattice[19] and to previous studies focusing on frustrated classical magnetism with ultracold bosons[20].

Our system relies on a lattice formed by the interference of two orthogonal retro-reflected laser beams whose relative phase is actively stabilized[21,22]. With equal beam intensities, this interference realizes a non-separable square lattice rotated by 45°. Tunable frustration is introduced by an extra tunnelling term t' along one diagonal of this square lattice (Fig. 1a) and controlled by the intensity imbalance between the two beams (Fig. 1b), in contrast to previous realizations of lattices with three beams and a 120° rotational invariance[18,20,23–25]. As a result, our geometry can be smoothly changed from a square lattice for $t'/t = 0$ to an isotropic triangular lattice at $t'/t = 1$ and undergoes a dimensional crossover to weakly coupled one-dimensional chains in the limit $t'/t \gg 1$.

We prepare a balanced mixture of fermionic ^{6}Li atoms in the two lowest hyperfine states into this tunable optical lattice by adiabatically

[1]Department of Physics, Harvard University, Cambridge, MA, USA. [2]Department of Physics, University of California, Davis, CA, USA. ✉e-mail: mgreiner@g.harvard.edu

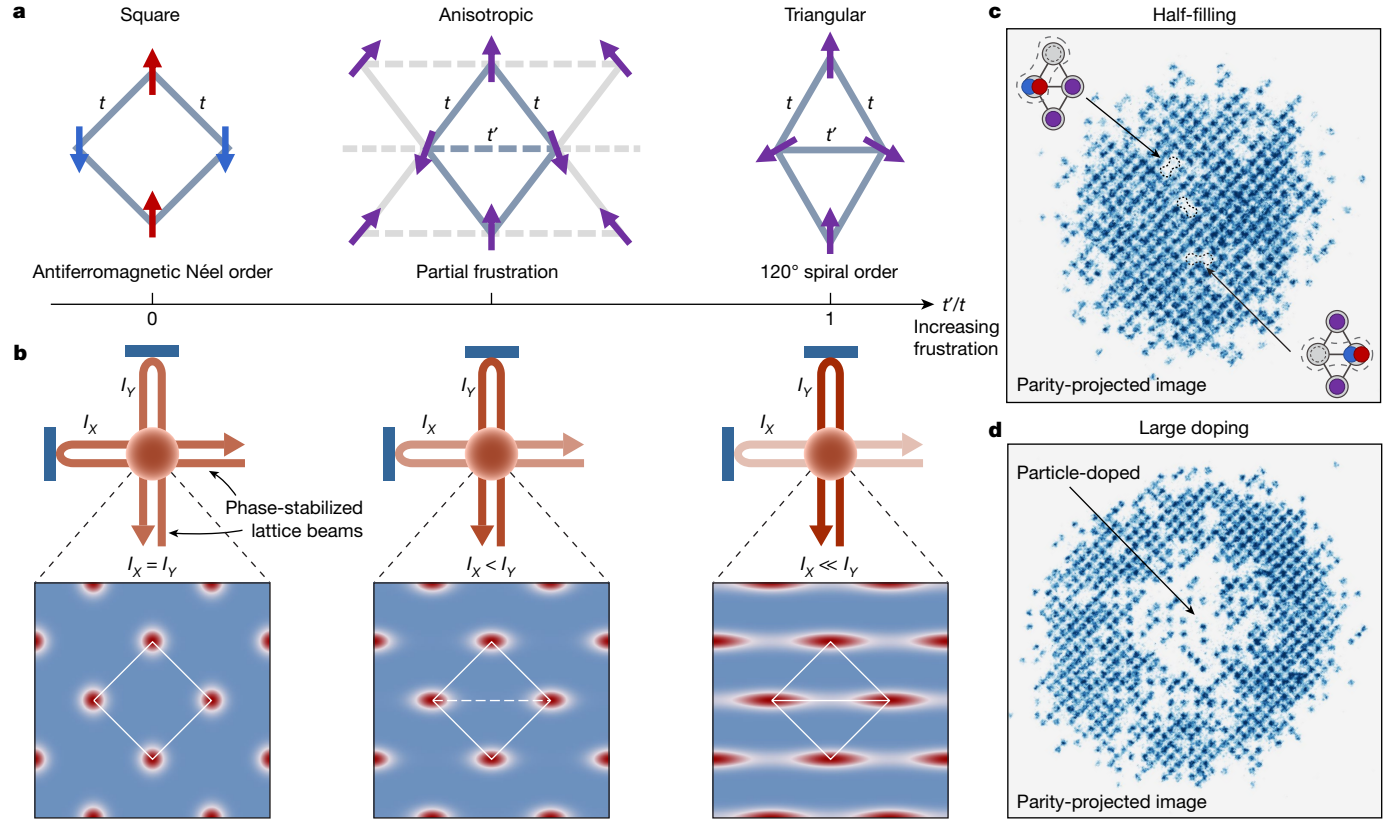

Fig. 1 | Investigating frustration on a tunable triangular lattice with a quantum gas microscope. a, A square lattice with coupling t can be continuously transformed into a triangular lattice with an extra tunable coupling t' along one diagonal. Frustration is parameterized by the anisotropy ratio t'/t and leads to a change in the magnetic ground state from an antiferromagnetic Néel order in the square lattice ($t'/t = 0$) to a 120° spiral order in the isotropic triangular lattice ($t'/t = 1$), in both the classical and quantum Heisenberg limits. **b**, We implement this tunable lattice with two orthogonal retro-reflected lattice beams actively phase-locked to each other[21]. Their interference results in a non-separable square lattice potential rotated by 45°. Adjusting the intensity balance between the lattice beams X and Y (I_X and I_Y) reduces the potential barrier between a pair of diagonal neighbours and enhances tunnelling. **c**, We realize a frustrated Fermi–Hubbard magnet by preparing a Mott insulator of about 500 fermionic atoms in the tunable lattice. Doublon–hole pairs appear owing to quantum fluctuations at our finite interaction energy $U/t \approx 9$ and are imaged as pairs of empty sites connected by tunnellings $t(')>0$ in a typical fluorescence picture owing to parity-projected imaging (with anisotropy $t'/t = 0.26(1)$). **d**, Atomic density varies across the sample owing to the presence of a radial confining potential, allowing us to locally investigate the effect of doping on magnetic order. With increasing the total atom number, a particle-doped region is imaged as a lighter disc inside a half-filled ring.

ramping the lattice powers within 160 ms. We set the s-wave scattering length to values $a_s = 358a_0 - 432a_0$ by tuning the magnetic bias field in the vicinity of the Feshbach resonance at 832 G, for which a_0 denotes the Bohr radius. The system is well described by a single-band Hubbard model with nearest-neighbour tunnelling $t = 355(11)–426(21)$ Hz and a tunable diagonal tunnelling $t' = 9.5(4)–370(6)$ Hz. Owing to the underlying harmonic confinement of the laser beams, atoms are subject to a trapping potential and show a spatially varying density n (Fig. 1d; see Methods).

Néel to spiral order transition

In the strong coupling limit at which U is greater than the bandwidth, the Hubbard Hamiltonian at half-filling can be approximated by an antiferromagnetic Heisenberg model with anisotropic spin exchange couplings $J(') = 4t(')^2/U$. This anisotropic spin model already features rich magnetic properties. In the bipartite square lattice $J' = 0$, the ground state is an antiferromagnetic Néel state[26]. By contrast, frustration in the isotropic triangular lattice gives rise to a 120° spiral Néel order[27–30]. Classical spin-wave theory predicts a transition between antiferromagnetic Néel order to an incommensurate spin spiral phase at $J'/J \geq 0.5$, which smoothly evolves into 120° order at $J'/J = 1$ (refs. 31,32). In the quantum spin-1/2 Heisenberg model, the location of the transition point is expected to be shifted above the classical value of 0.5 owing to quantum fluctuations, but its exact location is still an open question[33].

To shed light on the magnetic properties of the anisotropic triangular Hubbard model at intermediate U/t, we form a large Mott insulator of about 500 atoms by adjusting the local chemical potential at the centre of the trap to approximately reach half-filling (Fig. 1c). We measure the spin–spin correlation function

$$C_{\mathbf{d}}(\mathbf{r}) = \frac{1}{S^2}\left(\langle \hat{S}^z_{\mathbf{r}} \hat{S}^z_{\mathbf{r}+\mathbf{d}} \rangle - \langle \hat{S}^z_{\mathbf{r}} \rangle \langle \hat{S}^z_{\mathbf{r}+\mathbf{d}} \rangle\right) \quad (1)$$

between any pair of sites located at positions $\mathbf{r}$ and $\mathbf{r} \pm \mathbf{d}$, as described in our previous work[34]. We average this correlator within the central insulating region of about 200 sites, in which the chemical potential variation owing to harmonic confinement is minimal. In the square lattice $t'/t = 0.0265(3)$, we observe strong antiferromagnetic correlations decaying exponentially with distance (Fig. 2a, left), visible as a spatially averaged correlator $C_{\mathbf{d}}$ with a staggered sign that gradually fades out as a function of bond distance $\mathbf{d}$ in a logarithmic colour scale. Comparing the measured nearest-neighbour spin correlators to those obtained from determinant quantum Monte Carlo (DQMC) simulations at half-filling gives a fitted temperature of $T/t = 0.26(1)$.

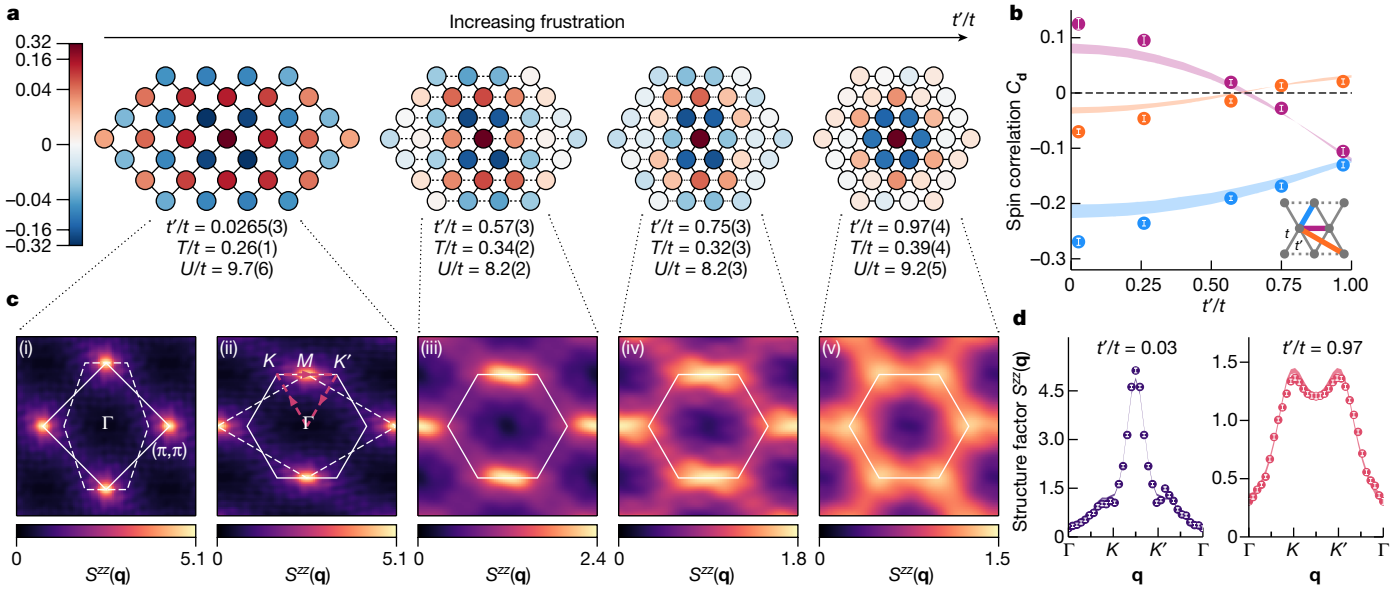

Fig. 2 | Frustrating short-range antiferromagnetic order in the square-to-triangular lattice transition. a, Real-space spin correlation $C_{\mathbf{d}}$ as a function of displacement **d** averaged over the region at half-filling. The magnitude of antiferromagnetic correlations decreases with increasing frustration, parameterized by t'/t, and the symmetry of the correlation function changes from fourfold D_4 to sixfold D_6, that is, hexagonal. Each panel is averaged over about 200 sites, with a typical s.e.m. of 0.005 (see Methods). The grid is smoothly stretched horizontally to emphasize the change in connectivity. **b**, Nearest-neighbour spin correlations across the t-bonds $C_{(1,0)}$, across the t'-bonds $C_{(1,1)}$ and next-nearest-neighbour correlation $C_{(2,1)}$. $C_{(1,0)}$ is decreasing with increasing frustration. $C_{(1,1)}$ and $C_{(2,1)}$ reverse sign as diagonal neighbours in the square lattice with aligned spins become nearest neighbours in the triangular lattice with antialigned spins. Shaded bands: DQMC simulations at $U/t = 9.5$ and $T/t = 0.35$–0.4. Experimental temperatures are lower than the DQMC data here for $t'/t = 0.0265(3)$ and $0.26(1)$. **c**, Measured spin structure factor $S^{zz}(\mathbf{q})$ plotted over the extended BZ of the square lattice (i) and triangular lattice (ii)–(v). (i),(ii), Antiferromagnetic order on the square lattice shows up as a single peak at quasi-momenta (π, π) in the square BZ and a peak at the M point of the hexagonal BZ. (ii)–(v), The single peak at the M point broadens with increasing t'/t and splits into two separate peaks at the K and K' points for $t'/t = 0.97(4)$. The broad peaks in (v) indicate short-range 120° order in the triangular lattice. **d**, Cut of the spin structure factor $S^{zz}(\mathbf{q})$ along the Γ–K–K′–Γ line (illustrated in **c**, (ii)). Shaded bands: DQMC simulations at $U/t = 9.7$, $T/t = 0.26$ (square) and $U/t = 9.2$, $T/t = 0.39$ (triangle), with widths propagated from experimental uncertainties (see Methods). The error bars denote one s.e.m. and the number of repetitions can be found in Methods.

As lattice anisotropy t'/t and frustration are increased, the growing superexchange coupling J' along the diagonal $\mathbf{d} = (1, 1)$ favours antialigned spins, which competes with the Néel ordering, favouring ferromagnetic correlation between sites on the same sublattice. As a result, we observe a suppression of the range of the spin–spin correlations. The correlator $C_{(1,1)}$ is furthermore weakened for moderate anisotropies $t'/t = 0.57(3)$ before changing its sign[35] (purple data points in Fig. 2b). In the configuration closest to the triangular geometry, $t'/t = 0.97(4)$, the three correlators to the nearest triangular neighbours $C_{(1,0)}$, $C_{(0,1)}$ and $C_{(1,1)}$ are consistently isotropic, with a residual difference by about 10% owing to technical limitations (see Methods). We also observe positive next-nearest correlations $C_{(2,1)}$ that reflect the effective hexagonal symmetry of the correlation function $C_{\mathbf{d}}$ that also show a sign change (orange data points, Fig. 2b). We observe a slight temperature increase as anisotropy t'/t is increased, to $T/t = 0.39(4)$ in the triangular lattice, which also contributes to the suppression of spin correlations dominated by frustration (see Methods). This heating may be because of increased laser noise with increasing lattice intensity imbalance.

In solid-state systems, magnetic transitions can be observed through changes in the symmetry of the spin structure factor, which can be measured, for example, by means of neutron scattering. Here we obtain the spin structure factor $S^{zz}(\mathbf{q})$ from the Fourier transformation of the real-space spin correlation function (see Methods). Antiferromagnetic Néel order in the square lattice appears as a well-defined peak at quasi-momentum (π, π), the M symmetry point of the first Brillouin zone (BZ) (Fig. 2c). As we increase t'/t, this peak becomes anisotropic, broadening along the K–K' direction. For the triangular lattice case, we observe two distinct peaks at the K and K' points of the hexagonal BZ, indicative of the 120° spiral order. The short-range character of this 120° order is evident from a global reduction and a broadening of the spin structure factor peaks (Fig. 2d).

Particle–hole asymmetry

Interactions between itinerant charge and magnetic moments can lead to rich collective quantum phases. One paradigm is doping a Néel-ordered Mott insulator, in which the interplay between the kinetic energy of the mobile dopants and strong correlations is believed to underlie the physics of cuprates. In the square lattice Hubbard model, however, Néel antiferromagnetism is made particularly robust at half-filling by Fermi surface nesting and the absence of geometric frustration, which may obscure competing orders. Doping frustrated systems in which intriguing phases already arise at half-filling may bring distinct new physics[11,13]. Anisotropic triangular lattices can be seen as the simplest lattice that frustrates collinear Néel order and breaks the particle–hole symmetry through a single diagonal next-nearest-neighbour tunnelling t'.

We investigate the effect of doping by increasing the central lattice filling to $n = 1.6$; together with a slow variation of the chemical potential resulting from the lattice confinement, this allows us to examine short-range spin correlations over a large range of both particle and hole dopings $\delta = n - 1$ in the local density approximation (see Methods). As expected from the particle–hole symmetry in the band structure (Fig. 3a), we find that the nearest-neighbour spin correlation $C_{(1,0)}$ in the square lattice remains antiferromagnetic and decays similarly on hole-doping or particle-doping $\pm\delta$ (Fig. 3b, bottom), with a residual asymmetry explained by deviations of the underlying confinement from a radially symmetric harmonic potential. By contrast, we observe

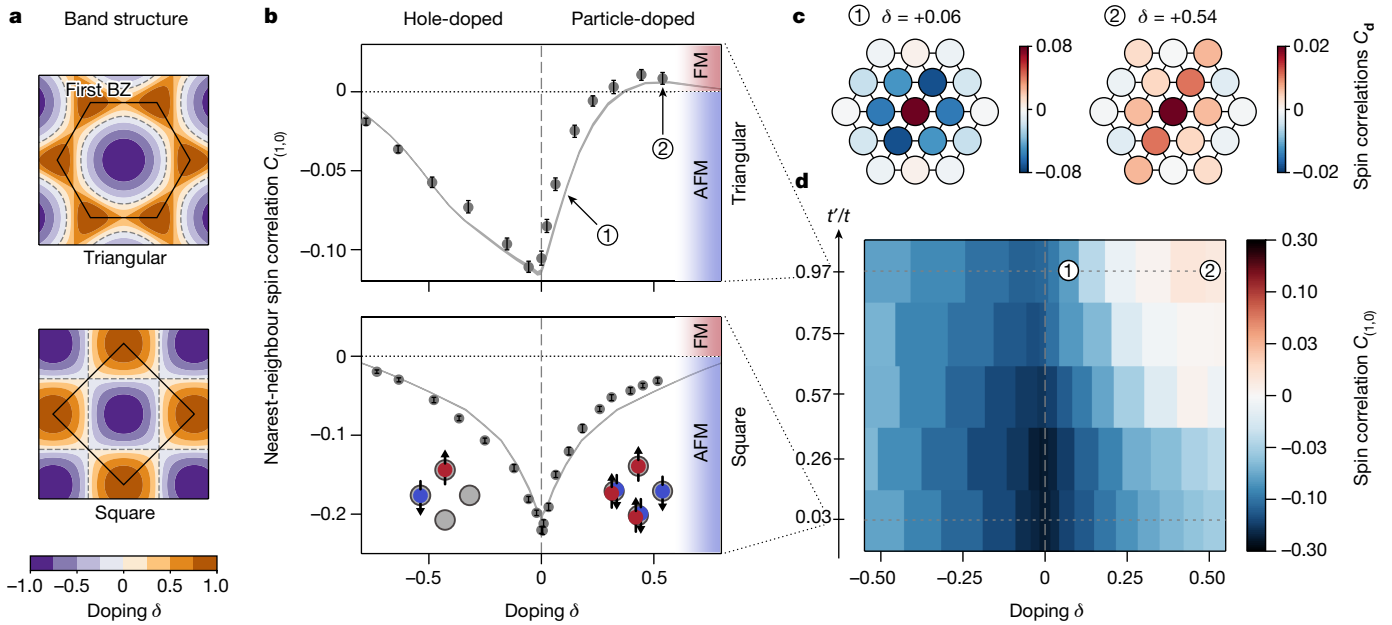

Fig. 3 | Particle–hole asymmetry of magnetic correlations and particle-doping-induced ferromagnetism. a, Particle–hole symmetry is broken in the triangular lattice, which is visible as a change of the shape and topology of the non-interacting band structure above (purple) and below (brown) half-filling. In the particle–hole-symmetric square lattice, antiferromagnetic order is enhanced at half-filling owing to a strongly nested square Fermi surface (dashed lines) for weak interactions. **b**, Doping leads to a decrease in the magnitude of the antiferromagnetic spin correlations averaged over the t lattice bonds $C_{(1,0)}$ and $C_{(0,1)}$ (grey points) compared with the half-filling value (vertical dashed line). A pronounced particle–hole asymmetry emerges in the triangular lattice, whereas the correlation function is symmetric in the square lattice. Grey lines show DQMC simulations at $U/t = 9.1$, $T/t = 0.44$ (triangular) and $U/t = 9.0$, $T/t = 0.40$ (square). **c**, Spin correlation maps in the triangular lattice at dopings $\delta = 0.06$ and $\delta = 0.54$. Nearest-neighbour correlations change to weakly ferromagnetic at $\delta = 0.54$ with values $C_{(1,0)} = 0.011(6)$ and $C_{(1,1)} = 0.006(5)$. **d**, Nearest-neighbour spin correlations over the t lattice bonds as a function of doping δ and lattice anisotropy t'/t, showing a large region of weakened correlations at positive doping and $t'/t > 0.5$. The error bars denote one s.e.m. and the number of repetitions can be found in Methods. AFM, antiferromagnetic; FM, ferromagnetic.

particle–hole-asymmetric magnetism in the nearly isotropic triangular lattice $t'/t = 0.97(4)$ (Fig. 3b, top). There, at the same temperature, antiferromagnetic correlations survive for a wide range of hole dopings, whereas they are strongly suppressed with particle doping. Surprisingly, we find that the correlator $C_{(1,0)}$ even becomes significantly ferromagnetic above a certain particle doping $\delta \gtrsim 0.2$, as confirmed in spin correlation maps (Fig. 3c).

Asymmetric spin correlations are to be expected for a Fermi liquid owing to the particle–hole asymmetry of the triangular lattice band structure: the shape and topology of the non-interacting Fermi surface changes markedly on increasing density and separates into two disconnected parts centred around the symmetry points K and K' close to full filling $n = 2$ (Fig. 3a). However, comparing with DQMC simulations, we note that the experimentally observed sign reversal at large particle dopings and sharp asymmetric suppression of spin correlation close to half-filling are absent in a non-interacting system (see Methods). The agreement with DQMC simulations at the experimental interaction strength $U/t = 9.2(5)$ suggests that this asymmetric interplay of particle and hole dopants with magnetism is unique to interacting systems (Fig. 3b, grey lines). This asymmetry and strongly weakened correlations at particle dopings $\delta \approx +0.5$ are similarly observed in anisotropic triangular geometries $t'/t \geq 0.57$ (Fig. 3d).

One possible mechanism for the particle–hole asymmetry in the stability of spin correlations can be understood by considering one dopant on a triangular plaquette in the superexchange energy $J(') = 0$ limit[36,37], similar to the Nagaoka effect[38]. The dopant could minimize its kinetic energy when different hopping paths interfere constructively, which is decided by the effective sign of the tunnellings $t(')$ and the surrounding spin configuration. With the sign convention of this work, a particle dopant has $t(') > 0$ and a spin triplet, ferromagnetic configuration allows the dopant to hop with constructive quantum interference. A hole dopant, by contrast, has an effective $t(') < 0$ and thus prefers a spin singlet, antiferromagnetic configuration. However, at finite $J(')$ and low temperatures $T \lesssim J(')$, as in our experiment, how such kinetic frustration competes with magnetic orders still remains an open question.

Particle–hole asymmetry is particularly apparent in spin correlations along the diagonal bonds $C_{(1,\pm1)}$ (Fig. 4a). In a square lattice, both correlators are equal, particle–hole-symmetric and show a reversal from positive to negative for dopings $|\delta| \gtrsim 0.2$ (ref. 34). As the anisotropy t'/t increases, the nature of $C_{(1,1)}$ changes from a next nearest neighbour to a nearest neighbour and its value smoothly interpolates to the particle–hole-asymmetric correlator $C_{(1,0)}$ in the triangular lattice (Fig. 3b). The ferromagnetic character of this correlator on particle doping is most pronounced at $t'/t \approx 0.5$ (Fig. 4b) and we find quantitative agreement with DQMC simulations. Notably, increasing the frustration parameter t'/t has the opposite effect on the other diagonal correlator $C_{(1,-1)}$, which becomes antiferromagnetic on particle doping (Fig. 4a, bottom).

Discussion and outlook

Possible scenarios for the appearance of ferromagnetism in the Hubbard model have been identified at the mean-field level[39], for single dopants[38] or at high temperature in frustrated systems[37,40], but a complete theoretical picture in our regime of temperatures $T \lesssim J$ and strong correlations is missing. The existence of a Van Hove singularity in the non-interacting density of states of the triangular lattice at a density $n = 3/2$, together with weak ferromagnetic correlations observed in DQMC simulations even at small interaction $U/t = 4$ (see Methods), could suggest that density of states may play a crucial role[41–45]. Experimentally, our findings might be related to recent observations in transition-metal-dichalcogenide moiré materials[46]. Quantum gas

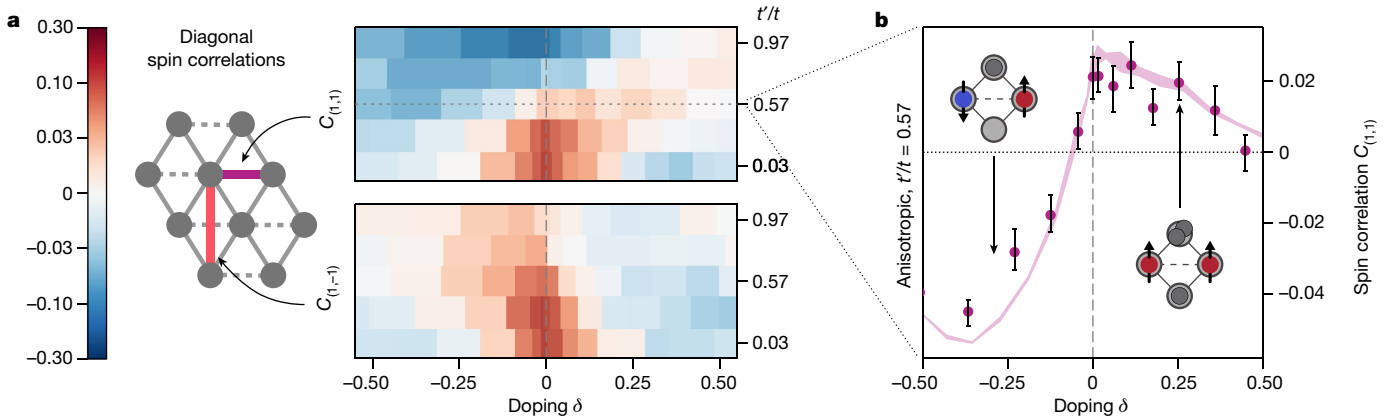

Fig. 4 | Next-nearest-neighbour spin correlations at finite doping. a, Spin correlations between next nearest neighbours $C_{(1,1)}$ (along the t' bond, purple) and $C_{(1,-1)}$ (diagonal, red) similarly show particle–hole asymmetry away from the square lattice geometry. **b**, In the anisotropic triangular lattice $t'/t = 0.57(3)$, correlations along the tunable triangular bond t' show a clear sign reversal from antiferromagnetic for hole doping $\delta < -0.1$ to ferromagnetic for $\delta \geq 0$. Purple lines show a DQMC simulation at $U/t = 9$ and $T/t = 0.4$. The error bars denote one s.e.m. and the number of repetitions can be found in Methods.

microscope experiments could help explain the microscopic processes underlying doping-induced magnetism through the measurement of spin–spin–charge correlations[47,48], as well as momentum-resolved spectroscopy[49].

Further experimental studies at interactions close to the metal-to-insulator transition would also help shed light on a conjectured spin liquid phase with broken time-reversal symmetry[8,50]. Moreover, through the addition of a third superlattice beam[21], our tunable experimental platform allows for exploring extensions of the Hubbard model directly related to cuprate materials, such as the t–t' model, which could help explain the emergence of superconducting phases with doping[14].

Online content

Any methods, additional references, Nature Portfolio reporting summaries, source data, extended data, supplementary information, acknowledgements, peer review information; details of author contributions and competing interests; and statements of data and code availability are available at https://doi.org/10.1038/s41586-023-06280-5.

1. Anderson, P. W. Resonating valence bonds: a new kind of insulator? *Mater. Res. Bull.* **8**, 153–160 (1973).
2. Balents, L. Spin liquids in frustrated magnets. *Nature* **464**, 199–208 (2010).
3. Zhou, Y., Kanoda, K. & Ng, T.-K. Quantum spin liquid states. *Rev. Mod. Phys.* **89**, 025003 (2017).
4. Williams, J. M. et al. Organic superconductors—new benchmarks. *Science* **252**, 1501–1508 (1991).
5. Kino, H. & Fukuyama, H. Phase diagram of two-dimensional organic conductors: (BEDT-TTF) 2X. *J. Phys. Soc. Jpn* **65**, 2158–2169 (1996).
6. Shimizu, Y., Miyagawa, K., Kanoda, K., Maesato, M. & Saito, G. Spin liquid state in an organic Mott insulator with a triangular lattice. *Phys. Rev. Lett.* **91**, 107001 (2003).
7. Laubach, M., Thomale, R., Platt, C., Hanke, W. & Li, G. Phase diagram of the Hubbard model on the anisotropic triangular lattice. *Phys. Rev. B* **91**, 245125 (2015).
8. Szasz, A., Motruk, J., Zaletel, M. P. & Moore, J. E. Chiral spin liquid phase of the triangular lattice Hubbard model: a density matrix renormalization group study. *Phys. Rev. X* **10**, 021042 (2020).
9. Motrunich, O. I. Variational study of triangular lattice spin 1/2 model with ring exchanges and spin liquid state in κ-$(ET)_2Cu_2(CN)_3$. *Phys. Rev. B* **72**, 045105 (2005).
10. Wietek, A. et al. Mott insulating states with competing orders in the triangular lattice Hubbard model. *Phys. Rev. X* **11**, 041013 (2021).
11. Zhu, Z., Sheng, D. N. & Vishwanath, A. Doped Mott insulators in the triangular-lattice Hubbard model. *Phys. Rev. B* **105**, 205110 (2022).
12. Lee, P. A., Nagaosa, N. & Wen, X.-G. Doping a Mott insulator: physics of high-temperature superconductivity. *Rev. Mod. Phys.* **78**, 17–85 (2006).
13. Song, X.-Y., Vishwanath, A. & Zhang, Y.-H. Doping the chiral spin liquid: topological superconductor or chiral metal. *Phys. Rev. B* **103**, 165138 (2021).
14. Pavarini, E., Dasgupta, I., Saha-Dasgupta, T., Jepsen, O. & Andersen, O. K. Band-structure trend in hole-doped cuprates and correlation with T_{cmax}. *Phys. Rev. Lett.* **87**, 047003 (2001).
15. Wannier, G. H. Antiferromagnetism. The triangular Ising net. *Phys. Rev.* **79**, 357–364 (1950).
16. Lee, P. A. An end to the drought of quantum spin liquids. *Science* **321**, 1306–1307 (2008).
17. Savary, L. & Balents, L. Quantum spin liquids: a review. *Rep. Prog. Phys.* **80**, 016502 (2016).
18. Yang, J., Liu, L., Mongkolkiattichai, J. & Schauss, P. Site-resolved imaging of ultracold fermions in a triangular-lattice quantum gas microscope. *PRX Quantum* **2**, 020344 (2021).
19. Mongkolkiattichai, J., Liu, L., Garwood, D., Yang, J. & Schauss, P. Quantum gas microscopy of a geometrically frustrated Hubbard system. Preprint at https://arxiv.org/abs/2210.14895 (2022).
20. Struck, J. et al. Quantum simulation of frustrated classical magnetism in triangular optical lattices. *Science* **333**, 996–999 (2011).
21. Tarruell, L., Greif, D., Uehlinger, T., Jotzu, G. & Esslinger, T. Creating, moving and merging Dirac points with a Fermi gas in a tunable honeycomb lattice. *Nature* **483**, 302–305 (2012).
22. Sebby-Strabley, J. et al. Preparing and probing atomic number states with an atom interferometer. *Phys. Rev. Lett.* **98**, 200405 (2007).
23. Jo, G.-B. et al. Ultracold atoms in a tunable optical kagome lattice. *Phys. Rev. Lett.* **108**, 045305 (2012).
24. Yamamoto, R., Ozawa, H., Nak, D. C., Nakamura, I. & Fukuhara, T. Single-site-resolved imaging of ultracold atoms in a triangular optical lattice. *New J. Phys.* **22**, 123028 (2020).
25. Trisnadi, J., Zhang, M., Weiss, L. & Chin, C. Design and construction of a quantum matter synthesizer. *Rev. Sci. Instrum.* **93**, 083203 (2022).
26. Hirsch, J. E. & Tang, S. Antiferromagnetism in the two-dimensional Hubbard model. *Phys. Rev. Lett.* **62**, 591–594 (1989).
27. Singh, R. R. P. & Huse, D. A. Three-sublattice order in triangular- and Kagomé-lattice spin-half antiferromagnets. *Phys. Rev. Lett.* **68**, 1766–1769 (1992).
28. Huse, D. A. & Elser, V. Simple variational wave functions for two-dimensional Heisenberg spin-½ antiferromagnets. *Phys. Rev. Lett.* **60**, 2531–2534 (1988).
29. Jolicoeur, T. & Le Guillou, J. C. Spin-wave results for the triangular Heisenberg antiferromagnet. *Phys. Rev. B* **40**, 2727–2729 (1989).
30. Capriotti, L., Trumper, A. E. & Sorella, S. Long-range Néel order in the triangular Heisenberg model. *Phys. Rev. Lett.* **82**, 3899–3902 (1999).
31. Trumper, A. E. Spin-wave analysis to the spatially anisotropic Heisenberg antiferromagnet on a triangular lattice. *Phys. Rev. B* **60**, 2987–2989 (1999).
32. Merino, J., McKenzie, R. H., Marston, J. B. & Chung, C. H. The Heisenberg antiferromagnet on an anisotropic triangular lattice: linear spin-wave theory. *J. Phys. Condens. Matter* **11**, 2965–2975 (1999).
33. Weihong, Z., McKenzie, R. H. & Singh, R. R. P. Phase diagram for a class of spin-½ Heisenberg models interpolating between the square-lattice, the triangular-lattice, and the linear-chain limits. *Phys. Rev. B* **59**, 14367–14375 (1999).
34. Parsons, M. F. et al. Site-resolved measurement of the spin-correlation function in the Fermi-Hubbard model. *Science* **353**, 1253–1256 (2016).
35. Chang, C.-C., Scalettar, R. T., Gorelik, E. V. & Blümer, N. Discriminating antiferromagnetic signatures in systems of ultracold fermions by tunable geometric frustration. *Phys. Rev. B* **88**, 195121 (2013).
36. Tasaki, H. The Hubbard model - an introduction and selected rigorous results. *J. Phys. Condens. Matter* **10**, 4353 (1998).
37. Morera, I. et al. High-temperature kinetic magnetism in triangular lattices. *Phys. Rev. Res.* **5**, L022048 (2023).
38. Nagaoka, Y. Ferromagnetism in a narrow, almost half-filled s band. *Phys. Rev.* **147**, 392–405 (1966).
39. Hirsch, J. E. Two-dimensional Hubbard model: numerical simulation study. *Phys. Rev. B* **31**, 4403–4419 (1985).
40. Haerter, J. O. & Shastry, B. S. Kinetic antiferromagnetism in the triangular lattice. *Phys. Rev. Lett.* **95**, 087202 (2005).
41. Hanisch, T., Kleine, B., Ritzl, A. & Müller-Hartmann, E. Ferromagnetism in the Hubbard model: instability of the Nagaoka state on the triangular, honeycomb and kagome lattices. *Ann. Phys.* **507**, 303–328 (1995).
42. Martin, I. & Batista, C. D. Itinerant electron-driven chiral magnetic ordering and spontaneous quantum Hall effect in triangular lattice models. *Phys. Rev. Lett.* **101**, 156402 (2008).

43. Merino, J., Powell, B. J. & McKenzie, R. H. Ferromagnetism, paramagnetism, and a Curie-Weiss metal in an electron-doped Hubbard model on a triangular lattice. *Phys. Rev. B* **73**, 235107 (2006).
44. Weber, C., Läuchli, A., Mila, F. & Giamarchi, T. Magnetism and superconductivity of strongly correlated electrons on the triangular lattice. *Phys. Rev. B* **73**, 014519 (2006).
45. Lee, K., Sharma, P., Vafek, O. & Changlani, H. J. Triangular lattice Hubbard model physics at intermediate temperatures. *Phys. Rev. B* **107**, 235105 (2023).
46. Tang, Y. et al. Simulation of Hubbard model physics in WSe_2/WS_2 moiré superlattices. *Nature* **579**, 353–358 (2020).
47. Koepsell, J. et al. Imaging magnetic polarons in the doped Fermi–Hubbard model. *Nature* **572**, 358–362 (2019).
48. Garwood, D., Mongkolkiattichai, J., Liu, L., Yang, J. & Schauss, P. Site-resolved observables in the doped spin-imbalanced triangular Hubbard model. *Phys. Rev. A* **106**, 013310 (2022).
49. Brown, P. T. et al. Angle-resolved photoemission spectroscopy of a Fermi–Hubbard system. *Nat. Phys.* **16**, 26–31 (2020).
50. Chen, B.-B. et al. Quantum spin liquid with emergent chiral order in the triangular-lattice Hubbard model. *Phys. Rev. B* **106**, 094420 (2022).

Methods

Hubbard model on anisotropic triangular lattice

In this work, we study the Hubbard model on anisotropic triangular lattices

$$\begin{aligned}\mathcal{H} = &-t\sum_{\mathbf{r},\sigma}\left(c^{\dagger}_{\mathbf{r}+(1,0),\sigma}c_{\mathbf{r},\sigma}+c^{\dagger}_{\mathbf{r}+(0,1),\sigma}c_{\mathbf{r},\sigma}+\text{h.c.}\right)\\ &-t'\sum_{\mathbf{r},\sigma}\left(c^{\dagger}_{\mathbf{r}+(1,1),\sigma}c_{\mathbf{r},\sigma}+\text{h.c.}\right)+U\sum_{i}n_{\uparrow}n_{\downarrow}\end{aligned} \tag{2}$$

with tunnelling t between sites $\mathbf{r}$ that are nearest neighbours on a square lattice and tunnelling t' along one diagonal $\mathbf{d} = (1, 1)$ tunable between 0 and t.

Here we take the convention in which $t(') \geq 0$. Thus, in the isotropic triangular lattice, the non-interacting energy band lies within $(-6t, 3t)$. U is the onsite interaction energy.

Experimental methods

Triangular optical lattice. We use two retro-reflected laser beams (X, Y) that are phase locked to each other to implement an interference lattice inside a glass cell. As described in previous works[51], each lattice beam is retro-reflected from a spherical mirror to form a standard standing wave and undergoes a further vertical reflection off a super-polished substrate. This reflection forms a one-dimensional lattice in the z direction with a larger spacing determined by the beam angle of incidence $\theta = 69.2(1)°$ on the substrate. We selectively load a two-dimensional atomic gas into a single layer of the z lattice, in which the two-dimensional lattice potential can be written as:

$$\begin{aligned}V(x,y) = &-\frac{V_x\bar{r}^4(1+\cos(2\theta))}{4}\cos(2k_x x)\\ &-\frac{V_y\bar{r}^4(1+\cos(2\theta))}{4}\cos(2k_y y)\\ &-\cos\phi\frac{\sqrt{V_xV_y}}{4}((1+\bar{r}^4)\bar{r}^2\cos^2\theta\cos(k_x x-k_y y)\\ &+2\bar{r}^4\cos^2\theta\cos(k_x x+k_y y))-\frac{V_x\bar{r}^2(1+\bar{r}^4)(1+\cos(2\theta))}{8}\\ &-\frac{V_y\bar{r}^2(1+\bar{r}^4)(1+\cos(2\theta))}{8}\end{aligned} \tag{3}$$

Here $k_x = k_y = 2\pi\sin\theta/\lambda$ are the horizontal lattice wavenumbers associated with the lattice wavelength $\lambda = 1{,}064$ nm. ϕ is the interference time phase between the X and Y lattice beams and is set to $\phi = 0$ or π to minimize the effect of phase fluctuations on the lattice potential. We thus form a non-separable square lattice rotated by 45° compared with the beam propagation directions, with a spacing $a = 805$ nm.

Each pass through a surface of the uncoated glass cell incurs a loss owing to Fresnel reflection; we calculate the reflection coefficient $r = 8.27(1)\%$ and transmission $\bar{r} = 1 - r$ from the calibrated beam angles and the light polarization. The polarization is chosen to be p-polarization relative to the plane of incidence on the substrate to maximize the interference between the two (X, Y) beams; this is close to s-polarization on the glass cell. We use V_x and V_y to denote the lattice depths if the polarization were horizontal (s on substrate) and without Fresnel loss. This notation is convenient when we need to take into account partial interference owing to polarization angle and losses.

To realize a tunable diagonal tunnelling $t' = 0$–1, we set the ratio between the intensities of the two lattice beams to $V_y/V_x \approx 1$–300. The strong imbalance reduces the potential barrier connecting neighbours along the diagonal $\mathbf{d} = (1, 1)$ to compensate the longer separation $\sqrt{2}a$ and enhances quantum tunnelling.

Lattice loading and imaging. The preparation of the ultracold Fermi gas before loading into optical lattices is similar to our previous works[34]. To load the gas into the interfering lattice, which we refer to as the physics lattice, we adiabatically perform a linear ramp of the lattice powers and hence of the lattice depths $V_{x,y}$.

We perform site-resolved imaging in a separate, dedicated lattice, which we will refer to as the imaging lattice. The imaging and physics lattice beams are overlapped on a polarizing beam splitter and are in orthogonal polarizations. The protocol used to take a site-resolved image is shown in Extended Data Fig. 1. We first ramp up the physics lattice depth to about $80E_R$ within 50 μs, with $E_R = h^2/8ma$ being the recoil energy. This fast ramp rapidly suppresses the tunnelling between lattice sites and allows for a faithful measurement of observables in the lattice occupation basis[52]. After freezing the density and spin distribution, we adiabatically transfer the atoms from the physics lattice to the imaging lattice with two hand-offs composed of three linear ramps, each of 20 ms in duration.

The imaging lattices are formed from the same laser source with a wavelength of 1,064 nm but their frequencies are detuned relative to each other and to the physics lattice to effectively cancel any interference term. This non-interfering lattice therefore has a two-dimensional square potential $V \propto -V_x\cos(2k_x x) - V_y\cos(2k_y y)$, which contains twice as many sites as the interfering physics lattice. To ensure a high fidelity transfer from the physics to the supersampling imaging lattice, it is important that each site of the physics lattice has good overlap with only one sublattice of the imaging lattice. If this is not the case, for example, if one physics site equally overlaps with two imaging sites, it is difficult to maintain adiabaticity in the transfer. We achieve this overlap condition by carefully choosing the frequency offset to compensate the phase shift induced by the reflection off the substrate for the Y beams. For the X beams, such a frequency offset turns out to be not enough and we choose to use a third $\overline{X}$ lattice to mediate the transfer: it has good overlap with both imaging and physics X lattices. We first transfer atoms from the physics lattice to $\overline{X}$ and then transfer to the imaging lattice, both with the linear ramp mentioned above. We selectively remove atoms in one of the hyperfine states as mentioned in previous work[34] in the imaging lattices.

Potential compensation. Owing to the imbalanced powers used on the X, Y axes in the triangular lattice, the harmonic confinement provided by the Gaussian envelope of the lattice beams is different along different lattice axes. To obtain a radially symmetric sample, and to enhance the density near the trap centre, we use a digital micromirror device to project a compensating paraboloid potential onto the atoms. This digital micromirror device and its light source have been described in previous work[53].

Calibrations

Lattice depth, angle and phase calibration. We first calibrate the depth of each lattice beam individually by performing amplitude modulation spectroscopy in deep lattices of around $50E_R$, as described in a previous work[51]. Because each beam forms two orthogonal standing waves from retro-reflection and vertical reflection on the substrate, we are able to measure two bandgaps between the ground band and the second excited band of each effective one-dimensional lattice. We then calculate the band structure of the single-beam lattice with the potential:

$$\begin{aligned}V_l(l,z) = &-\frac{V_l}{8}((1+\bar{r}^4)\bar{r}^2\cos(2\theta)\cos(2k_z z)\\ &+2\bar{r}^4\cos(2\theta)\cos(2k_l l)+\bar{r}^4\cos(2(k_l l+k_z z))\\ &+\bar{r}^4\cos(2(k_l l-k_z z)))-\frac{V_l}{8}\bar{r}^2(1+\bar{r}^4)\end{aligned} \tag{4}$$

Here l refers to the direction of propagation of the beam x or y and $k_z = k\cos\theta$ is the wavevector associated with the vertical standing wave. By fitting gaps obtained from the band-structure calculation to

the measured bandgaps, we obtain the bare lattice depths $V_{x,y}$ (equation (3)), as well as the incident angle $\theta = 69.2(1)°$.

All experiments are performed when the interference between the X and Y beams is maximized, that is, for a interfering time phase $\phi = 0$ or $\phi = \pi$. We interferometrically measure twice this phase 2ϕ after a round trip between the optical setup in which the phase measurement occurs and the retro-reflecting mirrors in which the lattices are created; as a result, the interfering phase ϕ is only known modulo π. To find the point of maximal interference, we scan the phase-lock point ϕ through more than a full 2π period electronically by changing the phase ϕ_p of a phase-shifter and take site-resolved images at each value. When $\phi = \pm\pi/2$, the X, Y interference term vanishes and the lattice changes from a chequerboard to a square lattice, $V(x, y) \approx V_x\cos(2k_x x) + V_y\cos(2k_y y)$. This change is clearly visible in site-resolved images as a sudden doubling of the detected density of atoms owing to the halving of the unit cell. As ϕ is scanned through $\pm\pi/2$, the atom population moves from one sublattice A to the other sublattice B. We use the atom population imbalance $\mathcal{I} = (p_A - p_B)/(p_A + p_B)$ to find out where the transition is, as in Extended Data Fig. 3. We then change the phase ϕ_p by π using the phase-shifter to get $\phi = 0$ or π.

To calibrate the interference terms between X and Y, we turn on both lattice beams and amplitude modulate one of them in the deep lattice limit of approximately $160E_R$. We perform a Lorentzian fit on the modulation spectrum to determine the bandgaps from the ground band to the three d bands of the horizontal two-dimensional lattice. These bandgaps are sensitive to the angle between the beams X and Y in the horizontal plane, which we deliberately tune away from 90° to partially compensate for a tunnelling anisotropy between the $X + Y$ and $X - Y$ directions associated with Fresnel losses. The angle difference α from 90° is obtained from a fit of the calculated two-dimensional band structure to the spectrum, fixing all independently calibrated parameters. We find $\alpha = 0.98(9)°$, for which the uncertainty mostly comes from the uncertainties on the fits to the bandgap frequencies.

Using the calibrated lattice parameters, we numerically compute the band structure of the two-dimensional interfering lattice at experimental powers (Extended Data Fig. 2). The values of the experimental tunnelling amplitudes are obtained in the tight-binding approximation from a Fourier transform of the lowest energy band and are reported in Extended Data Table 1. We also confirmed that all higher-order tunnellings are at least two orders of magnitude smaller.

Imaging fidelity. As described in the section 'Lattice loading and imaging', our imaging sequence consists of two parts: a transfer from the physics lattice to the imaging lattice and fluorescence imaging through Raman sideband cooling. We characterize the fidelity of the fluorescence imaging as described in our previous work[34] and find the fidelity of correctly determining the occupation of a lattice site to be 99.4(6)%.

Next, we measure the fidelity of the transfer process from the physics lattice to the imaging lattice as follows. We load atoms in a Mott insulating state with a large U/t to ensure unity filling and then perform the physics to imaging transfer, followed by the usual fluorescence imaging. We count the fraction of atoms that are transferred to the 'wrong' sublattice of the imaging lattice starting from the unit-filled Mott insulator and find this fraction to be 0.9(2)%. These are atoms that did not adiabatically follow the physics-imaging transfer and we account for them as a reduction in imaging fidelity. Overall, we report an imaging fidelity of 98.5(7)%.

Data analysis

Spin structure factor. The spin structure factor $S^{zz}(\mathbf{q})$ is obtained by performing a Fourier transform of the measured real-space spin correlation function $C_{\mathbf{d}}$:

$$S^{zz}(\mathbf{q}) = \sum_{\mathbf{d}}^{|\mathbf{d}|\leq d_{\max}} e^{i\mathbf{q}\cdot\mathbf{d}} C_{\mathbf{d}}. \quad (5)$$

Owing to the finite spin correlation length at our experimental temperatures, the spin correlations rapidly fall off with distance $|\mathbf{d}|$. Hence we truncate the Fourier sum up to a cutoff distance $d_{\max}$, chosen such that the further distance correlations are negligible and the structure factor has converged within error bars. For the square lattice case $t'/t = 0.0265(3)$, we keep up to $d_{\max} = 8$, whereas for all other values of t'/t, we keep only up to $d_{\max} = 5$. We use a finely spaced grid of momentum space points (q_x, q_y) to compute the structure factor, which is equivalent to zero-padding the correlation function for distances larger than $d_{\max}$. This does not add or alter any information contained in the structure factor, while making it easier to see the broadening of the peaks as well as the change of the symmetry from fourfold to sixfold.

In Fig. 2c, we show two different BZs, square BZ in (i) and hexagonal BZ in (ii)–(v). Here we describe how we plot the structure factor for these two BZs. Because our imaging lattice forms a square grid, we can label each lattice site with a row and column index (i, j). We can convert these indices to a physical distance $\mathbf{r}_{i,j}$ using the lattice unit vectors $\mathbf{e}_1$ and $\mathbf{e}_2$, that is, $\mathbf{r}_{i,j} = i\mathbf{e}_1 + j\mathbf{e}_2$. For the square Hubbard model with negligible t' tunnelling, it is natural to choose $\mathbf{e}_1$ and $\mathbf{e}_2$ to be the unit vectors of the square lattice, which are orthogonal to each other. This results in a square BZ. For the anisotropic Hubbard model with finite t' tunnelling, we instead choose $\mathbf{e}_1$ and $\mathbf{e}_2$ to be the unit vectors of the triangular lattice, which are 120° with respect to each other. This results in a hexagonal BZ. Writing the unit vectors in Cartesian coordinates, we have:

$$\mathbf{e}_1^{\mathrm{sq}} = \left(\frac{1}{\sqrt{2}}, \frac{-1}{\sqrt{2}}\right), \quad \mathbf{e}_2^{\mathrm{sq}} = \left(\frac{1}{\sqrt{2}}, \frac{1}{\sqrt{2}}\right),$$
$$\mathbf{e}_1^{\mathrm{tri}} = \left(\frac{1}{2}, \frac{-\sqrt{3}}{2}\right), \quad \mathbf{e}_2^{\mathrm{tri}} = \left(\frac{1}{2}, \frac{\sqrt{3}}{2}\right).$$

Magnetic correlation length. The spin correlation length that can be obtained through different fit methods is shown as a function of lattice anisotropy t'/t in Extended Data Fig. 5.

In the square lattice, we can directly fit to the real-space spin correlation function $|C(\mathbf{d})|$ a modified exponential function

$$f_{\mathrm{NL}\sigma}(|\mathbf{d}|) = \frac{A}{\sqrt{|\mathbf{d}|}}\exp\left(-\frac{|\mathbf{d}|}{\xi}\right) \quad (6)$$

with amplitude A and correlation length ξ as fit parameters and excluding the nearest neighbours owing to its singlet nature. This form is inspired from renormalization-group studies of the quantum Heisenberg model and the associated $(2 + 1)d$ nonlinear-σ model[54].

More generally, magnetic correlation lengths can be extracted from the peaks of the spin structure factor $S^{zz}(\mathbf{q})$. A simple, common fit function is the following Ornstein–Zernike form:

$$f_{\mathrm{OZ}}(\mathbf{q}) = \frac{A}{[(q_x - Q_x)\xi_x]^2 + [(q_y - Q_y)\xi_y]^2} + B \quad (7)$$

with amplitude A and background offset B. The correlation lengths ξ_x and ξ_y are the inverse of the full widths at half maximum of this Lorentzian function along directions $x = (1, 1)/\sqrt{2}$ and $y = (-1, 1)/\sqrt{2}$. For $t'/t = 0.03$ to 0.75, we fix the peak centre (Q_x, Q_y) to be the M point (π, π), corresponding to antiferromagnetic Néel order. In the triangular lattice $t'/t = 0.97$, we define the fit function as the sum of two Lorentzian functions centred on the K, K' points $(Q_x, Q_y) = \pm(2\pi/3, 2\pi/3)$ in the BZ of the underlying square lattice, corresponding to 120° Néel order, and reduce $\xi_{x,y}$ to a single fit parameter $\xi = \sqrt{2}\xi_x = \sqrt{3}\xi_y/2$ describing an isotropic correlation length in triangular lattice units.

Radial binning and doping data. The underlying harmonic confinement provided by the Gaussian envelope of the lattice beams causes the local chemical potential to decrease from the centre to the edge of the trap, which naturally leads to a spatially varying density n. To obtain density-resolved correlations (Figs. 3 and 4), we assume that the underlying confinement has elliptical equipotential lines, which includes two-dimensional harmonic potentials with unequal trapping frequencies. We group lattice sites according to the normalized anisotropic distance $r = \sqrt{(x/\sigma_x)^2 + (y/\sigma_y)^2}$, in which x and y are the site coordinates relative to the centre of mass of the atomic distribution along its long and short axes and σ_x and σ_y are the square roots of the second moments of the distribution. Measured densities n_s and spin correlations $C_\mathbf{d}$ are then averaged over each distance bin containing 50 sites and typically 500 experimental realizations (see Extended Data Table 2).

To investigate the effect of particle doping, we increase the atom number compared with measurements done at half-filling to reach centre densities of about $n = 1.6$ atoms per site. We are only able to detect the density of singly occupied sites n_{det} owing to light-assisted collisions during imaging[34] and, as a result, both particle-doped and hole-doped regions show detected densities below the half-filling value (Fig. 1d). We correct detected densities n_{det} according to imaging fidelities and assume that reflects the density of singly occupied sites n_s. To convert them into actual densities n and doping $\delta = n - 1$, we locate the half-filling radius r_{hf} associated with the bin with maximum detected density n_s^{hf} that separates the particle-doped core to the hole-doped periphery of the sample. Density in the hole-doped bins at radii $r > r_{hf}$ is then obtained from the linear approximation $n_h = n_s/n_s^{hf}$, whereas density in the particle-doped bins $r < r_{hf}$ is given as $n_p = 1 + n_s/n_s^{hf}$. This linear approximation holds particularly well at experimental temperatures $T/t \leq 0.5$ and deviates by at most $\Delta n = 0.01$ from the actual density for all lattice anisotropies t'/t, as estimated from DQMC simulations at $U/t = 10$.

Fitting U/t and T/t from DQMC. We obtain U/t by comparing experimental parity-projected single occupancy densities and spin correlations to DQMC simulations. The results for U/t are listed in Extended Data Table 1 and the results for T/t are listed in Extended Data Table 2, both as a function of anisotropy t'/t.

To obtain these values, we first examine the doped data, in which temperatures are higher and thus easier to access in DQMC. As described later in the section 'DQMC simulation', we perform DQMC simulations on a mesh of μ, U, T and t', with simulation parameters described. At each point in the mesh, we compute the particle density $n(\mu, U, T, t')$, the double occupancy $d(\mu, T, t')$ and the nearest-neighbour spin correlator $C_{(1,0)}(\mu, U, T, t')$. These data can be inverted to yield $U(n, C_{(1,0)}, d, t')$, $T(n, C_{(1,0)}, d, t')$ and $\mu(n, C_{(1,0)}, d, t')$. We perform this inversion by linear interpolation. To find U and T, we then analyse the doped experimental data as described in the section 'Radial binning and doping data'. For each t'/t value, we find the radial distance with the maximal single occupancy density n_s^{max}. We also measure $C_{(1,0)}$ at this distance. Computing the double occupancy as $d = (1 - n_s^{max})/2$, we then compute $U(1, C_{(1,0)}, d, t')$ and $T(1, C_{(1,0)}, d, t')$ from the interpolated DQMC data.

Because the lattice parameters are identical between the doped dataset and the half-filled dataset, we assume that U is the same in the two datasets (at fixed t'/t). We can then extract temperatures in the half-filled dataset using a procedure similar to the above. We perform DQMC simulations on a more restricted μ mesh centred near half-filling, but a larger T mesh to capture the lower temperatures in this dataset. We measure $C_{(1,0)}(U, T, t')$ at half-filling from DQMC, invert this to $T(C_{(1,0)}, t', U)$ by linear interpolation and then evaluate the inverted function at the experimentally measured $C_{(1,0)}$.

All error bars are obtained by linearly propagating the errors on experimental quantities through the interpolated DQMC data. We neglect systematic errors introduced by the interpolation, as well as statistical errors in DQMC, as they are negligible in comparison with the statistical errors contributed by experimental data.

One may also invert this technique to obtain predicted spin correlations as a function of (n, T, U, t') by interpolation. This is the method used to generate the DQMC curves in Fig. 2d. Error bars are obtained by numerically differentiating the result with respect to the input parameters and performing linear error propagation from U, T and t'. To further illustrate this technique, in Extended Data Fig. 4, we plot the analogue of Fig. 2a,c, obtained from interpolated DQMC data, namely, the correlation maps and spin structure factors at the experimental parameters.

Data summary. For data presented in Fig. 2, we prepare our sample with an average parity-projected density n_{det} of 0.89(2) at the centre to have a Mott insulator at half-filling in a region of about 200 sites, in which the effect of harmonic confinement is minimal. For the data presented in Figs. 3 and 4, we prepare our sample with an average parity-projected density of about 0.4, which corresponds to a particle density of 1.6.

Theory comparison

DQMC simulation. DQMC or auxiliary-field quantum Monte Carlo (or AFQMC) is a type of unbiased numerical method to study quantum many-body problems. We apply this algorithm to simulate the anisotropic Fermi–Hubbard model described in this work using the QUEST package[55]. This method can fail to converge at low temperatures because of the negative sign problem[56] for general fermion systems, such as square lattice Hubbard models away from half-filling or anisotropic triangular lattice Hubbard models at any filling because of lack of particle–hole symmetry. Reliable results could still be generated with sufficient statistical averaging for the coldest temperature data of triangular lattice Hubbard model in the scope of this work. However, the exponentially decreasing average sign makes it very costly to reach lower temperatures and improved methods may be required.

We perform the DQMC simulations on an 8×8 lattice with a Trotter step size $td\tau = 0.02$ and we vary the number of imaginary time slices L to change inverse temperature $\beta = 1/T = Ltd\tau$. Each run is generated with 5,000 warmup passes and 30,000 measurement passes. For temperatures $T/t = 0.4$, we average over 16 independent runs with different seeds to obtain reliable statistics and for temperatures $T/t = 0.35$, we average over 33 runs to compensate the reduced average sign. Comparing our results with ref. 35, the statistical error dominates over Trotter and finite system size errors.

Theory results with experiment parameters. We show spin correlation maps computed with DQMC as shown in Extended Data Fig. 4a for different anisotropies and same interaction strength U/t and temperature T/t as in the experiments (Fig. 2a). We could also compute the spin structure factor by Fourier transforming the theory-predicted spin correlations (Extended Data Fig. 4b). We find quantitative agreement between experiment and theory on the spin correlations.

We find that both the temperature and the entropy are increasing as anisotropy increases, as shown in Fig. 2b. We plot the theory-predicted spin correlations at constant entropy $S = 0.5644k_B$ per particle and $U/t = 9.8$ in Extended Data Fig. 8. The constant entropy data are from ref. 35.

To study the how spin correlation is affected by doping and frustration, we run DQMC simulations for density $n = 0$–2, anisotropy $t'/t = 1.0$ and $U/t = 0$, 2, 4 and 6 at $T/t = 0.4$, as shown in Extended Data Fig. 6, and for $U/t = 10$ at $T/t = 0.5$–0.9, as shown in Extended Data Fig. 7.

The particle–hole asymmetric spin correlations in the non-interacting case ($U/t = 0$) are qualitatively different. The nearest-neighbour correlations are negative for all densities owing to Pauli exclusion[57–59] and the peak of such antiferromagnetic correlation is shifted from half-filling $n = 1$ towards the hole-doped side. As interaction U is increased, antiferromagnetic correlations are suppressed around $n = 1.5$ and already turn

ferromagnetic at $U/t = 6$. The sign reversal for large particle doping in the isotropic triangular lattice becomes more prominent as temperature decreases.

Data availability

The datasets generated and analysed during this study are available from the corresponding author on reasonable request. Source data are provided with this paper.

Code availability

The code used for the analysis are available from the corresponding author on reasonable request.

51. Greif, D. et al. Site-resolved imaging of a fermionic Mott insulator. *Science* **351**, 953–957 (2016).
52. Kale, A. et al. Schrieffer-Wolff transformations for experiments: dynamically suppressing virtual doublon-hole excitations in a Fermi-Hubbard simulator. *Phys. Rev. A* **106**, 012428 (2022).
53. Mazurenko, A. et al. A cold-atom Fermi–Hubbard antiferromagnet. *Nature* **545**, 462–466 (2017).
54. Chakravarty, S., Halperin, B. I. & Nelson, D. R. Two-dimensional quantum Heisenberg antiferromagnet at low temperatures. *Phys. Rev. B* **39**, 2344 (1989).
55. Varney, C. N. et al. Quantum Monte Carlo study of the two-dimensional fermion Hubbard model. *Phys. Rev. B* **80**, 075116 (2009).
56. Iglovikov, V. I., Khatami, E. & Scalettar, R. T. Geometry dependence of the sign problem in quantum Monte Carlo simulations. *Phys. Rev. B* **92**, 045110 (2015).
57. Müller, T. et al. Local observation of antibunching in a trapped Fermi gas. *Phys. Rev. Lett.* **105**, 040401 (2010).
58. Sanner, C. et al. Suppression of density fluctuations in a quantum degenerate Fermi gas. *Phys. Rev. Lett.* **105**, 040402 (2010).
59. Cheuk, L. W. et al. Observation of spatial charge and spin correlations in the 2D Fermi-Hubbard model. *Science* **353**, 1260–1264 (2016).

Acknowledgements We thank A. Bohrdt, E. Demler, A. Georges, D. Greif, F. Grusdt, E. Khatami, I. Morera, A. Vishwanath and S. Sachdev for insightful discussions. We acknowledge support from NSF grant nos. PHY-1734011, OAC-1934598 and OAC-2118310; ONR grant no. N00014-18-1-2863; DOE contract no. DE-AC02-05CH11231; QuEra grant no. A44440; ARO/AFOSR/ONR DURIP grant no. W911NF2010104; the NSF Graduate Research Fellowship Program (L.H.K. and A.K.); the DoD through the NDSEG programme (G.J.); the grant DOE DE-SC0014671 funded by the US Department of Energy, Office of Science (R.T.S.); the Swiss National Science Foundation and the Max Planck Harvard Research Center for Quantum Optics (M.L.).

Author contributions M.X., L.H.K., A.K., Y.G., G.J. and M.L. performed the experiment and collected and analysed data. M.X. performed the numerical DQMC simulations based on code curated by and under the guidance of R.T.S. M.G. supervised the study. All authors contributed extensively to the interpretation of the results and production of the manuscript.

Competing interests M.G. is co-founder and shareholder of QuEra Computing.

Additional information

Correspondence and requests for materials should be addressed to Markus Greiner.

Peer review information *Nature* thanks Thomas Schäfer and the other, anonymous, reviewer(s) for their contribution to the peer review of this work.

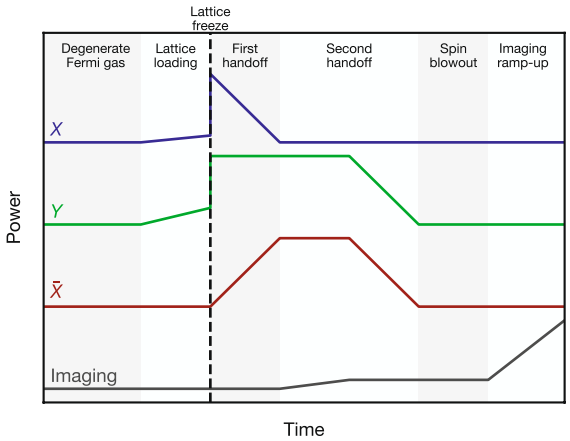

Extended Data Fig. 1 | Schematic of the lattice ramps used in the experimental protocol. We linearly ramp up the two physics lattice beams X and Y to experimental powers within 160 ms and quench them to freeze out dynamics. The X beam is handed over to an intermediate beam $\bar{X}$ by ramping down X and ramping up $\bar{X}$ simultaneously and then both $\bar{X}$ and Y beams are handed over to imaging beams by first ramping up the imaging beams and then ramping down the $\bar{X}$ and Y beams. All ramps use a 20-ms linear ramp. Optionally, one spin species can be removed with a resonant laser in the imaging lattice.

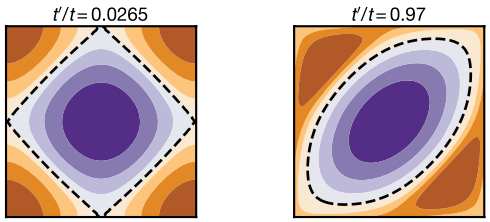

Extended Data Fig. 2 | Band structure for the full lattice potential from equation (3). Contour lines show the Fermi surface for different density levels in steps of $\Delta n = 1/4$. The dashed black line indicates half-filling. Hole-doped regions are shown in purple and particle-doped regions in brown.

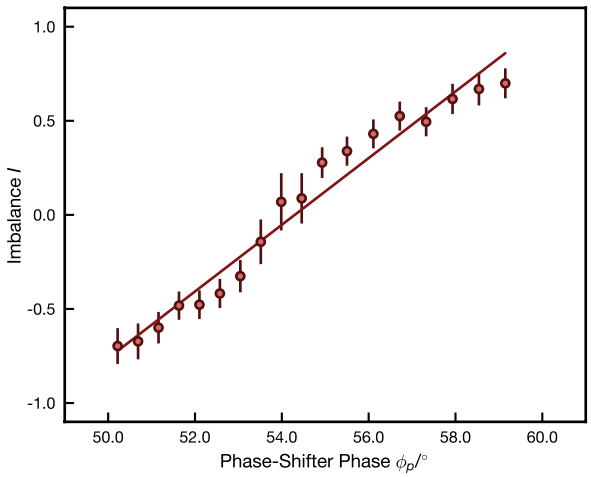

Extended Data Fig. 3 | Calibration of the interference phase. Atom number imbalance $\mathcal{I}$ between the two sublattices associated with potential (equation (3)), averaged over the whole cloud, as the interference phase ϕ is scanned using the electronic phase-shifter phase ϕ_p. We perform a linear regression to find out the phase ϕ_p at which the imbalance cancels, which corresponds to $\phi = \pi/2 \,(\mathrm{mod}\,\pi)$. The maximum interference phase $\phi = 0 \,(\mathrm{mod}\,\pi)$ is then obtained by increasing the phase-shifter phase ϕ_p by π.

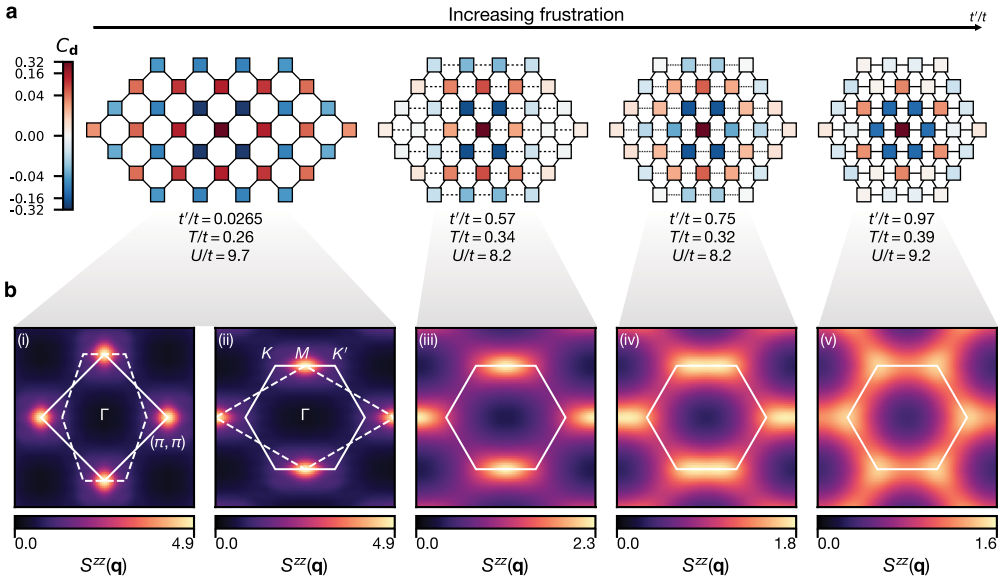

Extended Data Fig. 4 | Correlations at half-filling from the DQMC simulation. **a**, We plot the spin correlation functions from DQMC simulations on an 8 × 8 lattice as in Fig. 2a, at the same temperature T/t and interaction U/t as in experiments for each anisotropy t'/t. **b** The spin structure factors from DQMC are computed with the same interpolation method as in Fig. 2. The broadening of the spin structure factor peaks and its splitting in the isotropic triangular lattice agree quantitatively with the experiment.

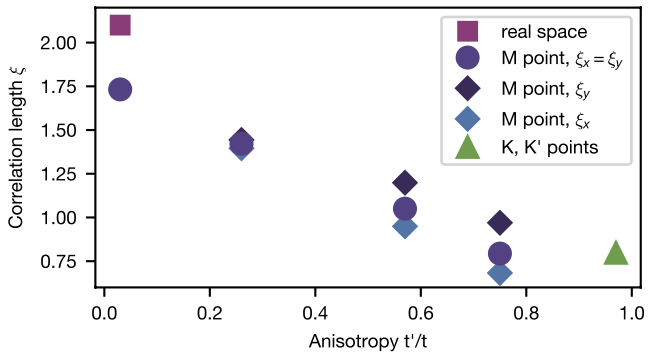

Extended Data Fig. 5 | Magnetic correlation length at half-filling. The correlation length is obtained from experimental data shown in Fig. 2 at different lattice anisotropies t'/t, by fitting the real-space spin–spin correlations $C_{\mathbf{d}}$ in the square lattice (square symbol) or the spin structure factor $S^{zz}(\mathbf{q})$ with an Ornstein–Zernike form at the M point (circles, isotropic form; diamonds, anisotropic form) or at the K and K' points (triangle). See text for details.

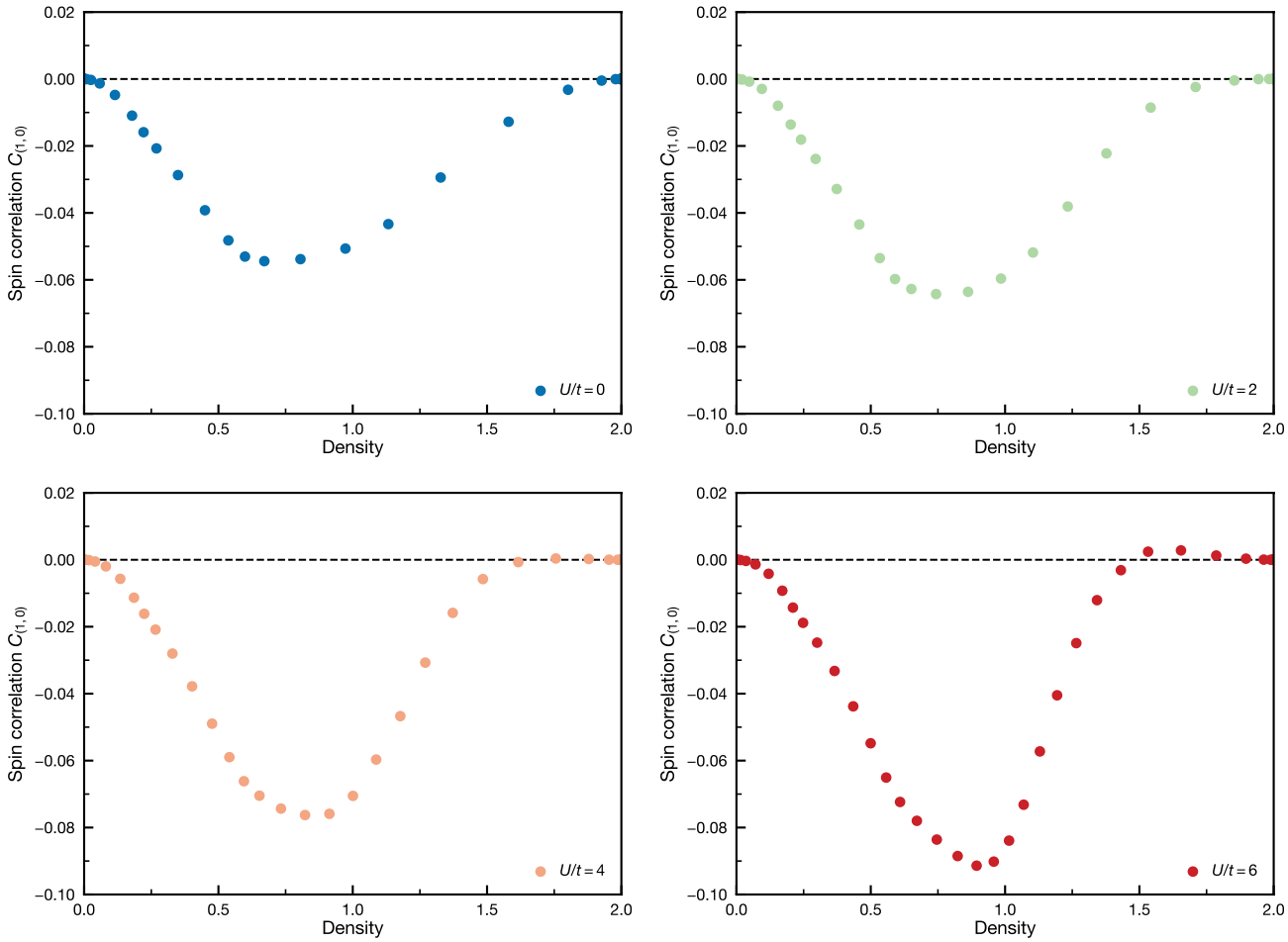

Extended Data Fig. 6 | Interaction dependence of the simulated spin correlations. The nearest-neighbour spin correlations $C_{(1,0)}$ are computed using DQMC for $t'/t = 1$, temperature $T/t = 0.4$ and for different interaction strengths $U/t = 0$, 2, 4 and 6. In the non-interacting case, the spin correlation is antiferromagnetic at all densities and decays to zero with a steeper slope on the hole-doped side than on the particle-doped side. As interaction U increases, the peak of correlation shifts towards half-filling and the slope of correlation is steeper on the particle-doped side. A sign reversal to ferromagnetic correlations is clearly visible at $U/t = 6$. Statistical error bars are smaller than the symbol size.

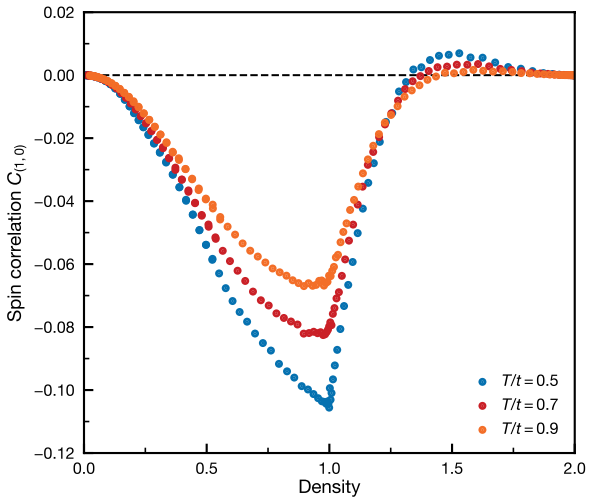

Extended Data Fig. 7 | Temperature dependence of the simulated spin correlations. The nearest-neighbour spin correlations $C_{(1,0)}$ are computed using DQMC for $U/t = 10$, $t'/t = 1$ and different temperatures $T/t = 0.5$–0.9 and show a clear particle–hole asymmetry. Statistical error bars are smaller than the symbol size.

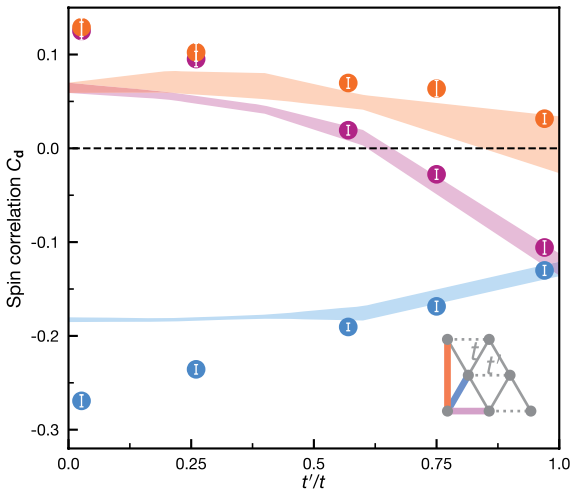

Extended Data Fig. 8 | Comparing experimental spin correlations with DQMC simulations at constant entropy. Nearest-neighbour spin correlations across the t-bonds $C_{(1,0)}$ (blue), across the t'-bonds $C_{(1,1)}$ (purple) and next-nearest-neighbour correlation $C_{(1,-1)}$ (orange) are shown, along with simulations at fixed entropy per particle $S = 0.5644 k_B$ (to be compared with Fig. 2b). The difference between experimental and simulated data hint at a larger entropy increase when preparing the system in a triangular lattice compared with a square lattice.

Extended Data Table 1 | Summary of tunnelling and Hubbard parameters

t'/t	t_x (Hz)	t_y (Hz)	t' (Hz)	U/t
0.0265(3)	355(11)	328(10)	9.5(4)	9.7(6)
0.26(1)	418(19)	392(18)	110(3)	8.9(4)
0.57(3)	426(21)	402(20)	245(5)	8.2(2)
0.75(3)	408(21)	386(20)	307(6)	8.2(3)
0.97(4)	380(20)	361(20)	370(6)	9.2(5)

Extended Data Table 2 | Summary of experimental temperatures and number of experiment realizations for each dataset

t'/t	Half-filling T/t	# of realisations, Fig. 2	Doped T/t	# of realisations, Figs. 3, 4
0.0265(3)	0.26(1)	432	0.35(1)	483
0.26(1)	0.33(1)	478	0.35(1)	635
0.57(3)	0.34(2)	613	0.39(2)	505
0.75(3)	0.32(3)	461	0.43(3)	495
0.97(4)	0.39(4)	953	0.47(6)	446